Electro-thermal mapping of polymer electrolyte membrane fuel cells with a fractal flow-field

V. S. Bethapudi [a, b], J. Hack [b], G. Hinds [c], P. R. Shearing [b], D. J. L. Brett [b, *], M. –O. Coppens [a, **]

[a] EPSRC "Frontier Engineering" Centre for Nature Inspired Engineering & Department of Chemical Engineering, University College London, London WC1E 7JE, United Kingdom

[b] Electrochemical Innovation Lab, Department of Chemical Engineering, University College London, London WC1E 7JE, United Kingdom

[c] National Physical Laboratory, Hampton Road, Teddington, Middlesex TW11 0LW, UK

Abstract

Electro-thermal maps of a polymer electrolyte membrane fuel cell (PEMFC) show the spatial distribution of current density and temperature, which is useful to evaluate their performance. Here, electro-thermal mapping is carried out for the first time on a PEMFC with a fractal cathode flow-field, the design of which emulates the efficient, scalable air transport inside the lungs. Such maps are compared with those of a conventional single-serpentine flow-field PEMFC. Each cell's performance is characterised by analysing the surface distribution of current density and temperature at different reactant relative humidity (RH) and cell voltage. Relationships are shown between segment current densities and surface temperatures, and between reactant relative humidity and cell operating conditions. The cells with a fractal flow-field deliver better electrochemical performance and exhibit more homogeneous current distributions compared to those with a single-serpentine flow-field, in which the current distribution is non-uniform due to cell flooding. The surface temperatures

23 are higher in cells with a fractal flow-field than in those with a single-serpentine flow-field,

24 consistent with the observed cell performances. In addition, electrochemical impedance

25 spectroscopy characterisation indicates flooding in the single-serpentine cells, but not in the

26 fractal cells.

29 * Corresponding author.

30 d.brett@ucl.ac.uk

31 Professor of Electrochemical Engineering

32 Department of Chemical Engineering

33 University College London

34 Torrington Place

35 London, WC1E 7JE

36 ** Corresponding author.

37 m.coppens@ucl.ac.uk

38 Ramsay Memorial Professor

39 Department of Chemical Engineering

40 University College London

41 Torrington Place

42 London, WC1E 7JE

43

44

45

1. Introduction

Polymer electrolyte membrane fuel cells (PEMFCs) operating on hydrogen, with no emissions at the point of use, are gaining prominence as alternatives to energy devices powered from fossil energy. PEMFCs supply uninterrupted power, as long as sufficient fuel (hydrogen) and oxidant (air) are supplied to support the electrochemical reactions. This is an advantage of PEMFCs compared to batteries, which cannot support continuous operation, due to their periodic charging needs. The electrical efficiency of PEMFCs can go as high as 60% and the overall efficiency can be further improved if the PEMFC is operated in combined heat and power mode [1,2]. For the successful and efficient functioning of PEMFCs, several components associated with their operation must work optimally. Of these, flow-fields play a vital role in the transport and the distribution of reactants to the electrodes, where the electrochemical reactions occur.

PEMFC flow-fields are categorised based on the geometrical configuration of their reactant flow channel path. The serpentine flow-field geometry is a commonly used channel configuration that provides reactant flow to the electrode surface, uniform stack compression and effective water and thermal management [3]. However, the serpentine flow-field has a relatively long reactant flow path that often results in concentration gradients and pressure drop along its length [4]. In addition, stagnation of liquid water along the serpentine flow paths can occur, resulting in mass transfer-related issues, such as channel flooding and reactant starvation that reduce the overall cell performance [5,6].

Lung-inspired, fractal flow-fields ("fractal cells" for short) have been identified to deliver better performance (higher electrical power) compared to those with conventional single-serpentine flow-fields, while overcoming the aforementioned issues related to flow

69 distribution [7–10]. The design of lung-inspired flow-fields [7–10] is based on rigorously

70 proportioned, scale-invariant structural features that lead to optimally efficient air transport

71 inside lungs, as opposed to biomimetic designs that are developed either by copying apparent

72 features of biological transport structures, such as veins, lungs and leaves, or by integrating

73 flow mechanisms observed in nature into conventional flow-field geometries, like serpentine,

74 interdigitated and parallel configurations for air transport [11–13]. Theoretical studies on

75 lung-inspired flow-fields by Kjelstrup, Coppens, Pharoah and Pfeifer [7] predicted that a 2D

76 planar fractal flow distributor could more uniformly distribute air over the membrane-

77 electrode assembly (MEA) region, compared to a serpentine flow-field, but also do so in a

78 thermodynamically optimal way. This study did not simply mimic biology, but applied

79 geometric features of the upper airway tree of mammalian lungs, which are scalable and

80 commensurate with minimum entropy production, to design fractal flow-fields for fuel cell

81 applications [7,14]. Trogadas et al. [8], Cho et al. [9], and Marquis et al. [15] carried out

82 numerical simulations incorporating three-dimensional finite element models of the flow-

83 fields and gas diffusion layers (GDLs), in combination with two-phase agglomerate models for

84 the catalyst layers, to study the effects of the GDL thickness and the number of fractal

85 branching generations on the PEMFC performance. These numerical simulations confirmed

86 analytical predictions that the ideal number of branching generations, N, is between $N = 5$

87 and $N = 7$ for a flow-field plate with a surface area of 10 cm^2, such that convection-dominated

88 flow and diffusion-controlled transport are balanced at both the outlets and the inlets (Péclet

89 number, Pe ≈ 1) [8,9]. Prototypes of lung-inspired cathode flow-fields with, first, 10 cm^2 and,

90 then, 25 cm^2 effective MEA area were built on the basis of the computationally assisted

91 designs discussed in [8,9]. These 3D branching fractal flow-field plates were fabricated using

92 selective laser sintering of stainless steel [8]. It was shown that a fractal cell with $N = 4$

93 generations delivered a higher power density compared to a single-serpentine cell of the

94 same MEA area at 50% and 75% reactant relative humidity (RH) conditions. It also

95 demonstrated 50% lower values in pressure drop compared to the conventional single-

96 serpentine flow-field design for all RH conditions tested. However, for both 10 cm^2 and 25

97 cm^2 cells, the fractal cell's performance degraded considerably under 100% RH conditions,

98 where additional water saturation occurred in the electrodes and the flow-field channels,

99 resulting in mass transport issues due to flooding. In addition, when fractal cells having N = 5

100 generations were tested, water flooding was observed during operation, irrespective of the

101 reactant conditions. This is due to ineffective water removal from the fractal cells, which limits

102 their usage at higher reactant humidity. Furthermore, current disadvantages related to using

103 selective laser sintering for flow-field manufacturing are the complexity and cost involved.

104 A novel method of 3D fractal flow-field development using 2D planar printed circuit board

105 (PCB) plates with a layer-wise assembly approach by Bethapudi et al. [10,16] overcame the

106 flooding issues and fabrication disadvantages associated with the previous designs [8]. Here,

107 a fractal flow-field was developed, with air outlet paths modified from the previous design,

108 which delivered superior performance to conventional single-serpentine cells under different

109 operating conditions, even at 100% reactant RH. The performance enhancement in the fractal

110 cell has been characterised and established by polarisation, temperature, galvanostatic and

111 electrochemical impedance measurements.

112 Current and temperature mapping have been instrumental for the *in situ* diagnosis and

113 analysis of various factors that affect the performance of fuel cells, such as water

114 management [17–19], reactant concentration and distribution [5,18,20,21], operating

115 conditions [22,23], flow channel configurations [24], thermal management [25–27] and cell

116 compression [28,29]. Some of the current distribution measurement techniques include

117 indirect correlations based on local values [30], use of magnetic effects and Hall sensors

118 [31,32], dependent on local potential measurements at the GDL and catalyst layer, and

119 segmented measurement [33]. Temperature distribution measurement techniques include

120 thermocouple insertions [34], infrared imaging [26,35] and segmented measurement. Of

121 these, segmented measurements have been identified as a particularly powerful technique,

122 especially for combined current and temperature measurements, due to their ability to

123 characterise localised phenomena, such as reactant starvation and flooding inside the fuel

124 cell [17,35,36]. Furthermore, PCB-based segmented current collectors are widely used in the

125 combined measurement of current and temperature, due to their low cost, flexibility during

126 assembly and disassembly and ability to perform *in situ* measurements within cells
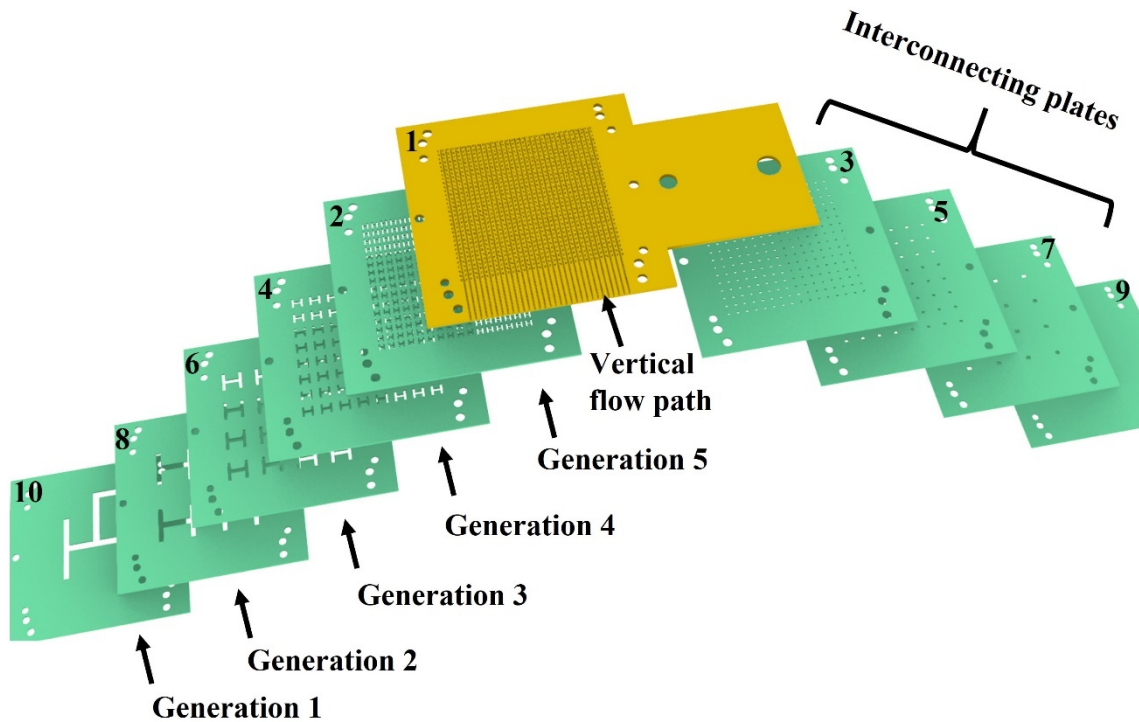
127 [20,25,37,38].

128 As discussed, previous studies have identified the benefits of fractal fuel cell cells, compared

129 with conventional single-serpentine cells [8,10,39]. These studies were primarily dependent

130 on using *in situ* electrochemical diagnostic techniques that established better hydration

131 distribution and regulation inside the fractal cells, and their associated cell performance. In

132 this study, design, development, and testing of a scaled-up layer-wise printed circuit board

133 (PCB) based cathode fractal flow-field, compared to the previous PCB based lung-inspired

134 flow-field with $N = 5$ fractal generations is presented. Simultaneous current and temperature

135 mapping are used to understand the reasons for the improved performance and investigate

136 the role of reactant RH and operating conditions, in addition to conventional electrochemical

137 performance tests. Segment currents are evaluated and analysed to understand the impact

138 of hydration distribution on the local currents generated in the cell, which provides new

139 insights and should help to guide further design, scale-up, and operation improvements of

140 fractal fuel cells.

2. Experimental setup and characterisation methods

2.1 Flow-field design

143 The cathode fractal flow-field was developed using a layer-wise printed circuit board (PCB)

144 plate technique, an approach that has been identified as cost-effective, easy and scalable for

145 manufacturing [10]. Several layers of 2D planar PCB plate, with each plate consisting of a

146 particular generation of the fractal flow-field structure, as shown in Fig. 1, were assembled to

147 produce a cathode flow-field with 3D hierarchical, fractal geometry. The cathode fractal flow-

148 field used here employed a 5-generation hierarchical fractal structure, with the airflow

149 through this flow-field occurring from a single inlet to 1024 outlets, covering an effective MEA

150 area of 25 cm^2. Each of the 5th generation outlets had dimensions of 400 μm × 800 μm, with

151 a spacing of 1.18 mm between adjacent outlets. Furthermore, a surface vertical flow path of

152 0.5 mm in both width and depth ran through this spacing.

Figure 1: Schematic outline and order of 2D planar PCB plates (generations and interconnecting plates) used for the development of a 5-generation cathode fractal flow-field plate. Plate 1: gold-coated; plates 2 – 10: plain PCB plates.

These surface paths act as the flow outlet for reactant air and water generated in the cathode region, making this flow-field an open-ended cathode fractal flow-field. A total of 10 PCB plates were used, with 6 plates (1, 2, 4, 6, 8 and 10) accommodating the 5 generations of the fractal structures, and 4 plates (3, 5, 7 and 9) acting as interconnecting plates between generations, respectively (Fig. 1). Plate 1, which adjoins the MEA, was gold-coated and acted as the cathode current collector for this flow-field, while all other plates (2 — 10) were plain PCB plates. Similarly, the cathode single-serpentine flow-field was developed using PCB plates with a 1 mm^2 square cross-sectional area single-serpentine channel with a depth of 1 mm and acted as the cathode current collector. Additional plain PCB plates were introduced with the cathode single-serpentine flow-field to ensure that the overall thickness of the single-serpentine and fractal flow-fields remained the same. Furthermore, vertical flow paths having 0.5 mm width and 1 mm depth were provided in the cathode single-serpentine flow-field,

169 with a spacing of 1.18 mm between them, for the removal of reactant air and product,

170 including crossover water. The effective MEA area covered by the cathode single-serpentine

171 flow-field was 25 cm^2. The corresponding cathode fractal and cathode single-serpentine flow-

172 fields are shown in Fig. S1.

173 The corresponding anode flow-field (Fig. 2) was constructed from a graphite plate of 3 mm in

174 thickness. Here, graphite was used because of its high electrical and thermal conductivity,

175 which facilitates current and temperature distribution measurements in the cells. The anode

176 flow-field had a single-serpentine square channel with an area of 1 mm^2 and a depth of 1 mm.

177 Besides, the anode current collector used was a gold-coated PCB plate.

178 **2.2 Flow-field fabrication**

179 The different flow-field features discussed above were fabricated using a Roland-40 CNC

180 setup (Roland, USA). In the cathode fractal flow-field, plate 1 had a 35 μm thick Cu coating

181 that was modified by first electroplating Ni from 0.13 M $Ni(SO_3NH_2)_2$ solution at 4.3 mA cm^{-2}

182 (corresponding to between 3 V — 3.5 V applied voltage) for 3 min. It was then electroplated

183 with Au from 0.02 M $KAu(CN)_2$ solution at 2.4 mA cm^{-2} (corresponding to between 3.5 V —

184 3.7 V applied voltage) for 70 min. The Au-coated plate (1) and plain plates (2 — 10) were hot

185 press assembled at 400 psig and 150 °C for 60 min, followed by a cooling phase of 120 min.

186 Prepreg polymer sheets were used for adhesion between the PCB plates. The final assembled

187 PCB cathode fractal flow-field had dimensions of 7.25 mm × 80 mm × 80 mm and is shown in

188 Supplementary Information Fig. S1. Similarly, the cathode single-serpentine flow-field was Ni-

189 and Au-coated, followed by a hot press assembly process, as above. The thickness of the

190 cathode single-serpentine flow-field was similar to that of the fractal flow-field to ensure

191 identical insulation levels in both cells. The final assembled cathode single-serpentine flow-

192 field with dimensions is also shown in Supplementary Information Fig. S1.

193 The anode flow-field had a single-serpentine square channel with an area of 1 mm^2 and a

194 depth of 1 mm drilled on a 3 mm thick graphite plate. The dimensions of the final fabricated

195 graphite-based anode single-serpentine flow-field were 3 mm x 80 mm x 80 mm. The anode

196 current collector was developed from a PCB plate, having a 35 µm thick Cu coating and was

197 coated with Ni and Au layers, using the aforementioned process.
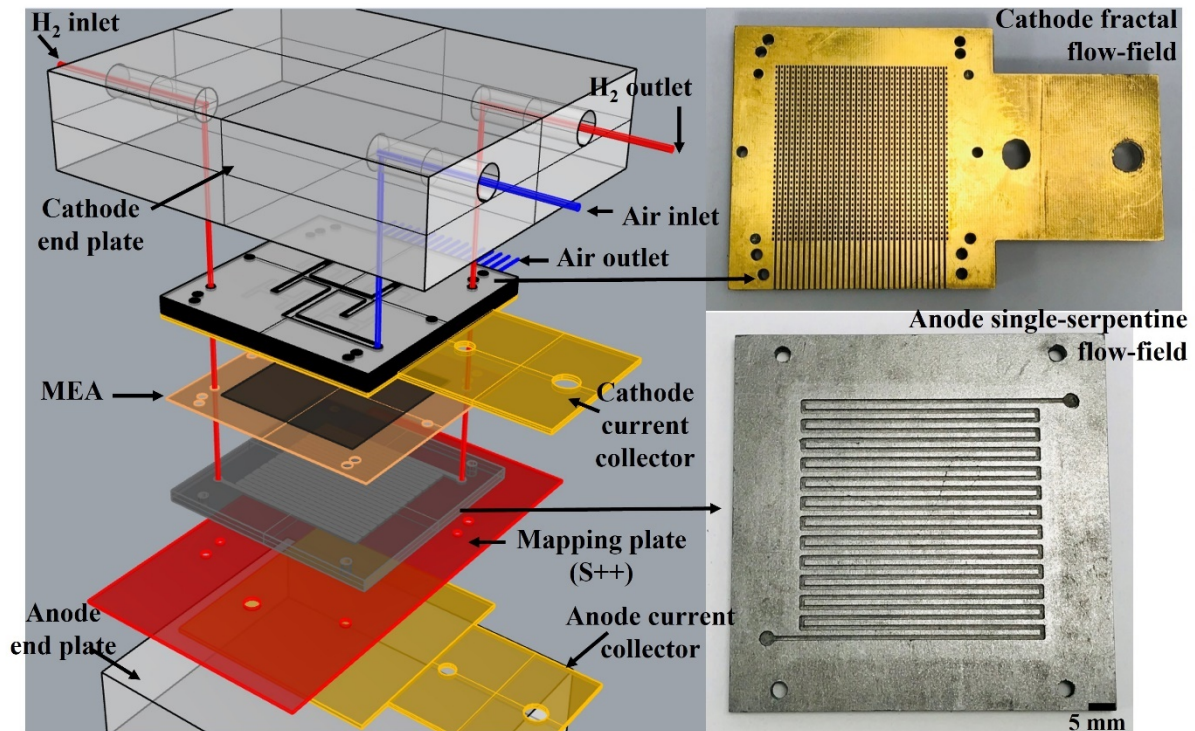
2.3 MEA preparation

199 The MEA used for fuel cell testing had an effective area of 25 cm^2. The membrane used was

200 Nafion® 212 (Dupont, USA) and the gas diffusion electrodes (GDEs) used were Hyplat Pt

201 catalyst (HyPlat, South Africa) coated with a catalyst loading of 0.4 mg$_{Pt}$ cm^{-2}. The gas diffusion

202 layer (GDL) used was a carbon paper-based Freudenberg H23C9 with PTFE-treated

203 microporous layer. The MEA components were hot pressed for 3 min at 400 psig and 150 °C,

204 and the final assembled MEA had a thickness of approximately 500 µm. Two Tygaflor gaskets

205 with a thickness of 250 µm were used to prevent gas leakage by sandwiching the MEA

206 between them.

2.4 Fuel cell assembly

208 The fuel cell components and their order of assembly are shown in Fig. 2. The current-

209 temperature mapping plate, S++ (S++ Simulation Services, Germany), was sandwiched

210 between the anode flow-field and anode current collector. It is noteworthy that the mapping

211 plate cannot be sandwiched at the cathode side, due to the electrically insulating nature of

212 the PCB plates. Besides, the current collection on the cathode plate occurs via the surface. In

213   contrast, the mapping plate requires through-plane electrical conduction, which is possible

214   with a conductive graphite plate on the anode side.

215   The S++ plate consisted of an array of 10×10 integrated shunt resistors, with each resistor

216   having an area of 5×5 mm^2, covering a total electrode area of 25 cm^2. The current

217   measurements were made in through-plane mode. The surface temperature distribution

218   measurement was carried out using a 5×5 array of temperature sensors. Current and

219   temperature measurements were made simultaneously, and their respective sensors were

220   located on the same sensor plate, made of PCB with Au-coated contact segments. The S++

221   plate was connected to a computer via a USB interface that provided live mapping

222   (current/temperature) display and data recording. The reactants, air and H$_2$, are supplied to

223   the cell as shown in Fig. 2. Air for both cathode fractal and cathode single-serpentine cells

224   exited from the surface vertical flow paths (horizontal blue lines in Fig. 2) into the ambient

225   atmosphere (Supplementary Information Fig. S1), while the H$_2$ outlet occurred from a

226   manifold, as shown in Fig. 2. The corresponding air and H$_2$ flows are represented by blue and

227   red lines, respectively, in Fig. 2. Compression of the cell components was provided using

228   aluminium end-plates (cathode and anode), with a nut and bolt arrangement tightened to a

229   torque of 1.4 N·m. The anode end-plate also acted as a heating device providing the necessary

230   start-up temperature to the cells, which was 45 °C. The cell temperature was measured using

231   a K-type thermocouple located within the anode flow-field plate.

232

Figure 2: Assembly outline and primary components used in the PEMFCs tested.

2.5 X-ray computed tomography (CT) scan

X-ray computed tomography (CT) scans were performed on the fractal cathode flow-field

using a Nikon XT – H 225 instrument (Nikon Metrology, UK). The corresponding experimental

setup, scan parameters, acquisition conditions, and the software utilised for data processing

and image reconstruction are discussed in previous work [10].

2.6 Fuel cell testing

A Scribner 850e testing station (Scribner Associates NC, USA) was used to test the fuel cells.

The testing station supplied the reactants at the desired temperature, reactant humidity (RH)

and flowrates. The RH of the reactants was maintained by the test station by considering the

cell temperature feedback and adjusting the corresponding reactant supply temperature. The

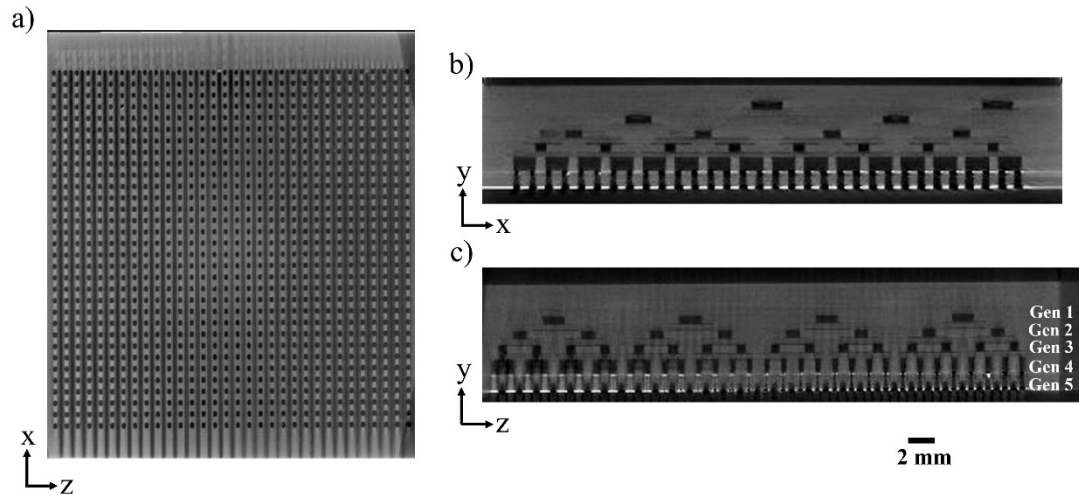fuel cells were supplied with hydrogen of 99.995% purity at a constant flow rate of 200 mL

245 min^{-1}, while the cathode airflow stoichiometry was maintained at 3.0. The cells were operated

246 under ambient cooling conditions. After each experimental condition, the cells were flushed

247 using nitrogen gas for 30 min on both cathode and anode regions of the cell to remove the

248 excess water and reactants present inside it. Detailed experimental parameters are given in

249 Table S1.

250 Electrochemical impedance spectroscopy (EIS) measurements were performed using a Gamry

251 Reference 3000 and Gamry Reference 30k Booster (Gamry Instruments, USA). The frequency

252 range for analysis was from 100 kHz to 0.1 Hz, with 10 points per decade and an AC

253 modulation amplitude of 5% of the DC input signal.

254 **3. Results and discussion**

255 **3.1 X-ray CT scan analysis**

256 X-ray CT scan imaging of the fractal flow-field was performed to analyse the internal structure

257 of the 5 generations of hierarchical fractal flow-field and the layer-wise cell assembly quality.

258 The corresponding zx, xy and zy virtual slices are shown in Fig. 3a, 3b and 3c, respectively.The

259 corresponding slice-by-slice 3D track through of the fractal flow-field in the zx, xy and zy

260 directions can be accessed by clicking on Fig. 3. The dark regions, where the attenuation is

261 lower, correspond to the flow channels, while the bright regions, where the attenuation is

262 higher, correspond to the PCB material. The dark vertical lines observed in Fig. 3a correspond

263 to the vertical flow paths, as shown in Fig. 2, which remove the excess reactants and product

264 water from the cell. The five hierarchical fractal generations can be identified distinctly in Figs.

265 3b and 3c. Overall, the inter-channel arrangement, individual layer assembly and hierarchical

266 flow paths are observed to be unobstructed, without any overlap, which establishes the PCB

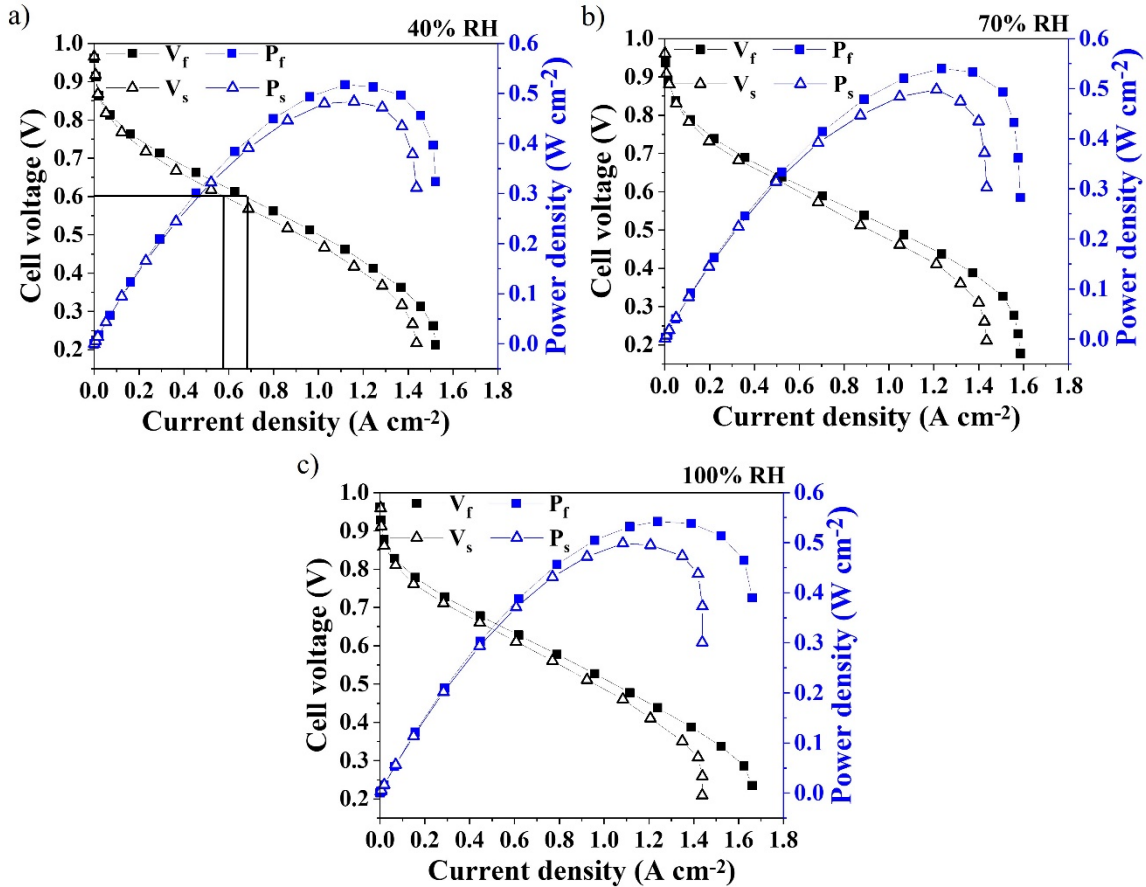267 layer-wise assembly approach to be an effective method for developing fractal flow-fields.

268

Figure 3: Virtual slices in the (a) zx plane showing the 5th generation flow outlets and vertical flow paths, (b) xy plane and (c) zy plane showing the hierarchy extending over five generations for the studied fractal cathode flow-field.

3.2   Polarisation performance

The polarisation performance of the single-serpentine and fractal cells under different operating conditions are compared in Fig. 4. It can be observed that the electrochemical performance of the fractal cell is better than that of the single-serpentine cell in the range of reactant RH tested. For instance, at 0.6 V cell voltage, which is often considered to be an optimal operating point in the trade-off between efficiency and power [10], the corresponding current density output at 40%, 70% and 100% RH for the fractal cell is 0.65 A cm^{-2}, 0.68 A cm^{-2} and 0.75 A cm^{-2}, and for the single-serpentine cell is 0.54 A cm^{-2}, 0.63 A cm^{-2}, and 0.68 A cm^{-2}, respectively. Furthermore, the limiting current densities at 40%, 70% and 100% RH for the fractal cell are 1.52 A cm^{-2}, 1.59 A cm^{-2} and 1.66 A cm^{-2}, compared to 1.44 A cm^{-2}, 1.43 A cm^{-2} and 1.42 A cm^{-2} for the single-serpentine cell.

14

Figure 4: Polarisation curves for the fractal cell and single-serpentine cell at (a) 40% reactant RH conditions, (b) 70% reactant RH conditions and (c) 100% reactant RH conditions. Legend: V_f – voltage of fractal cell, V_s – voltage of single-serpentine cell, P_f – power density of fractal cell and P_s – power density of single-serpentine cell.

The overall enhanced performance of the fractal cell can be attributed to its fractal geometry-based cathode flow-field structure, where a hierarchically structured flow channel with equal hydraulic path lengths between inlet and outlet allows for the transition of airflow from a convection-dominated state at the inlet to a more diffusion-dominated state at the outlets, resulting in more uniform distribution of reactants over the MEA surface [7,8,10,40]. The effects of more uniform reactant distribution at the cathode of the fractal cell can be identified from its superior performance over the single-serpentine cell, especially in the high current density region between 1.2 A cm^{-2} and 1.6 A cm^{-2}, where mass transport limitations occurring from reduced oxygen concentration in the cell are predominant, as shown in Fig. 4.

297   In addition to the more uniform reactant distribution, the presence of vertical flow paths

298   (Supplementary Information Fig. S1) in the fractal cell act to regulate the excess water away

299   from the MEA more effectively, avoiding excess stagnation of liquid water throughout the

300   system [10]. As a result, while the performance of the single-serpentine cell does not vary

301   appreciably with RH in the mass transport region, the performance of the fractal cell increases

302   with reactant RH, which can be attributed to a reduced level of flooding and reactant (oxygen)
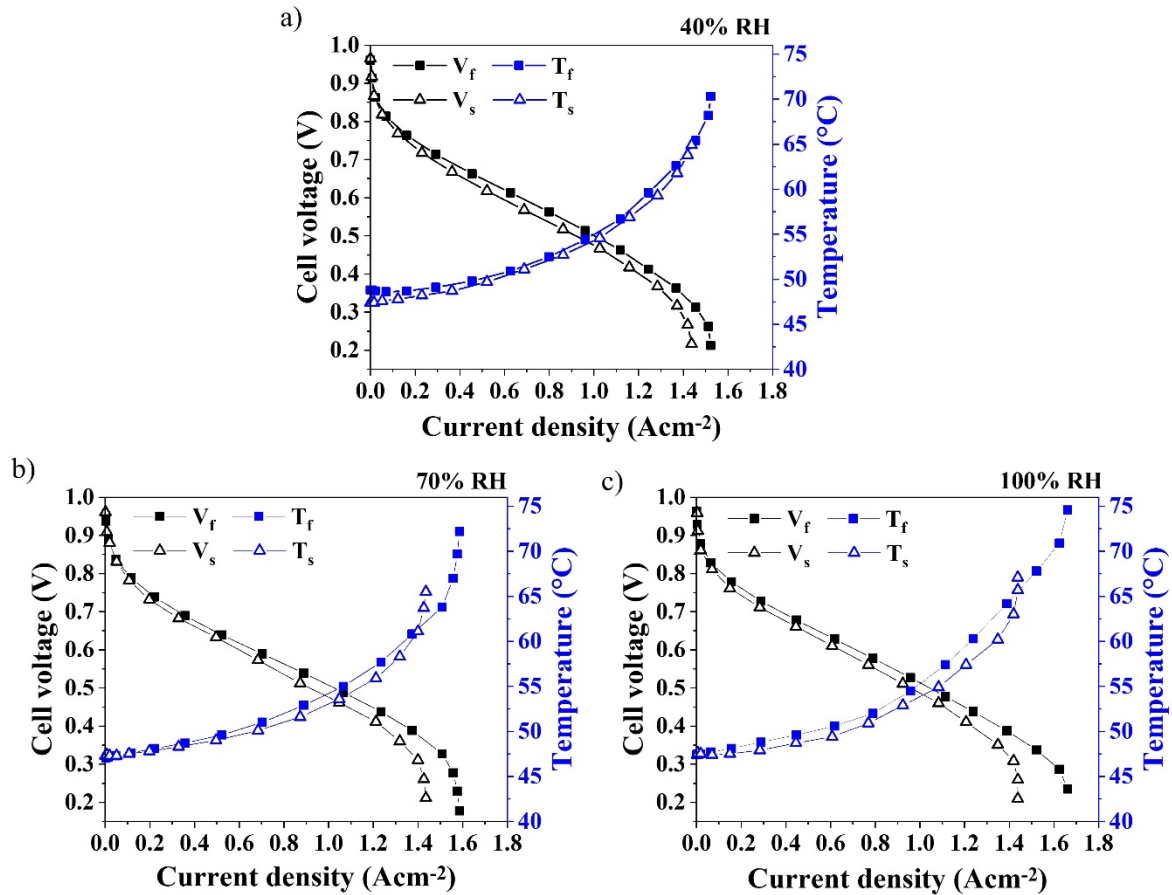
303   starvation [10,41].

304   *Table 1: Polarisation performances (current density) of fractal and single-serpentine cells at*
305   *0.6 V and 0.4 V cell voltages, and at 40%, 70% and 100% reactant RH conditions.*

PEMFC configuration	Cell voltage	Current density (A cm^{-2}) at 40% RH	Current density (A cm^{-2}) at 70% RH	Current density (A cm^{-2}) at 100% RH
Fractal	0.6 V	0.65	0.68	0.75
	0.4 V	1.25	1.35	1.37
Single-serpentine	0.6 V	0.54	0.63	0.68
	0.4 V	1.17	1.23	1.24

306

3.3 Cell temperature analysis

308   The increase in cell temperature, recorded during the polarisation curve measurements in

309   Fig. 4, is shown for each cell as a function of reactant RH in Fig. 5.

16

Figure 5: Simultaneous cell temperatures recorded during polarisation curve measurements, as in Fig. 4, using a single point thermocouple on the surface of the anode flow-field plate for the fractal cell and single-serpentine cell at (a) 40% reactant RH conditions, (b) 70% reactant RH conditions and (c) 100% reactant RH conditions. Legend: V_f – voltage of fractal cell, V_s – voltage of single-serpentine cell, T_f – temperature of fractal cell and T_s – temperature of single-serpentine cell.
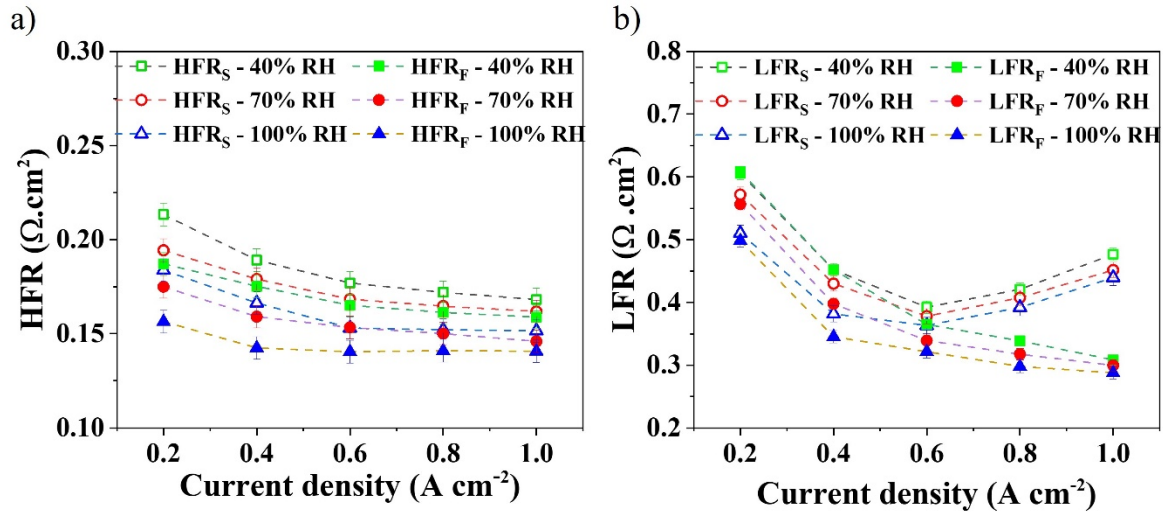
The maximum cell temperature developed (at the limiting current density) in the fractal and single-serpentine cells, at 40%, 70% and 100% RH, are 70.3 °C, 72.2 °C and 74.6 °C and 64.9 °C, 65.5 °C and 67.1 °C, respectively. It can be observed that the fractal cell exhibited higher operating temperatures under all conditions, especially in the high current density region, compared to the single-serpentine cell. It is well established that the degree of liquid water saturation has a notable influence on the cell temperature developed [42].

Increased water retention in the cathode region reduces the current density generated and leads to a corresponding decrease in cell temperature and *vice versa* [5]. Thus, the lower cell

325   temperatures in the single-serpentine cell can be attributed to the presence of excess water

326   saturation (flooding) inside the cell, despite operating at lower cell voltages compared to the

327   fractal cell [43].

328   **3.3 Electrochemical impedance spectroscopy (EIS) measurements**

329   EIS was performed on the fractal and single-serpentine cells over a range of current densities

330   and the corresponding Nyquist curves are given in Supplementary Information Fig. S2. The

331   corresponding high frequency resistance (HFR) or ohmic resistance developed in the cells is

332   given in Fig. 6(a). HFR is measured from the high frequency intercept of the Nyquist plot with

333   the real axis [44]. It primarily reflects the membrane hydration state and its associated

334   conductivity [45]. Fig. 6(a) shows that an increase in the reactant humidity from 40% RH to

335   70% RH and later to 100% RH results in a decrease in the HFR at the same current density,

336   which can be attributed to the improved membrane conductivity with increasing RH. The HFR

337   for each cell decreased with increasing current density, which can be attributed to improved

338   membrane hydration as a result of the increased amount of water generated via the higher

339   rate of the electrochemical reaction at the cathode. Overall, the observed trends in HFR are

340   a well-established phenomenon that is common to both flow-fields and suggests that both

341   cells were sufficiently hydrated throughout. The results also indicate that the level of

342   hydration is higher in the fractal cell at all the RH levels tested [46,47]. Low frequency

343   resistance (LFR), as shown in Fig. 6(b), is derived by fitting the Nyquist curves (Fig. S2) to an

344   equivalent circuit given in Fig. S3 and corresponds to the total resistance developed in a cell

345   [48].

Figure 6: (a) High frequency resistance (HFR or Ohmic) for fractal and single-serpentine cells at 40%, 70% and 100% RH reactant conditions and (b) low frequency resistance (LFR or total resistance) for fractal and single-serpentine cells at 40%, 70% and 100% RH reactant conditions. Legend - HFR$_s$ – HFR of single-serpentine cell, HFR$_F$ – HFR of fractal cell, LFR$_s$ – LFR of single-serpentine cell, LFR$_F$ – LFR of fractal cell.

For both cells, an initial decrease in LFR with increasing current density, as seen in Fig. 6(b), can be attributed to improved membrane hydration due to water generation at the cathode. This gradual reduction in LFR for both cells is observed between 0.2 A cm^{-2} and 0.6 A cm^{-2}. At low and intermediate current densities, the LFR, at 40%, 70% and 100% RH, for the single-serpentine and fractal cells are similar, with, at 0.2 A cm^{-2}, 0.60 Ω cm^2, 0.57 Ω cm^2, 0.51 Ω cm^2 (single-serpentine) and 0.61 Ω cm^2, 0.55 Ω cm^2, 0.49 Ω cm^2 (fractal), and, at 0.6 A cm^{-2}, 0.39 Ω cm^2, 0.37 Ω cm^2, 0.36 Ω cm^2 (single-serpentine) and 0.36 Ω cm^2, 0.33 Ω cm^2, 0.32 Ω cm^2 (fractal). The LFR and HFR decreased between 0.2 A cm^{-2} and 0.6 A cm^{-2}, as shown in Fig. 6(a). However, when the current density increases to 0.8 A cm^{-2} and further to 1 A cm^{-2}, a sudden rise in LFR for the single-serpentine cell is observed. This higher LFR for the single-serpentine flow-field at higher operating currents can be attributed to the increased charge- and mass transport related resistances, such as reactant starvation occurring from cell flooding [49]. The corresponding charge transfer resistances (R_{ct}) and mass transfer resistances (R_{mt}) for the

365   single-serpentine and fractal cells at 0.8 A cm^{-2} and 1 A cm^{-2} current densities are given in

366   Table 2. In contrast, the LFR for the fractal cell continues to decrease throughout its operation,

367   even in the high current density region, where R_{ct} and R_{mt} of the fractal cell are significantly

368   lower than for the single-serpentine cell, which can be attributed to the flooding-free,

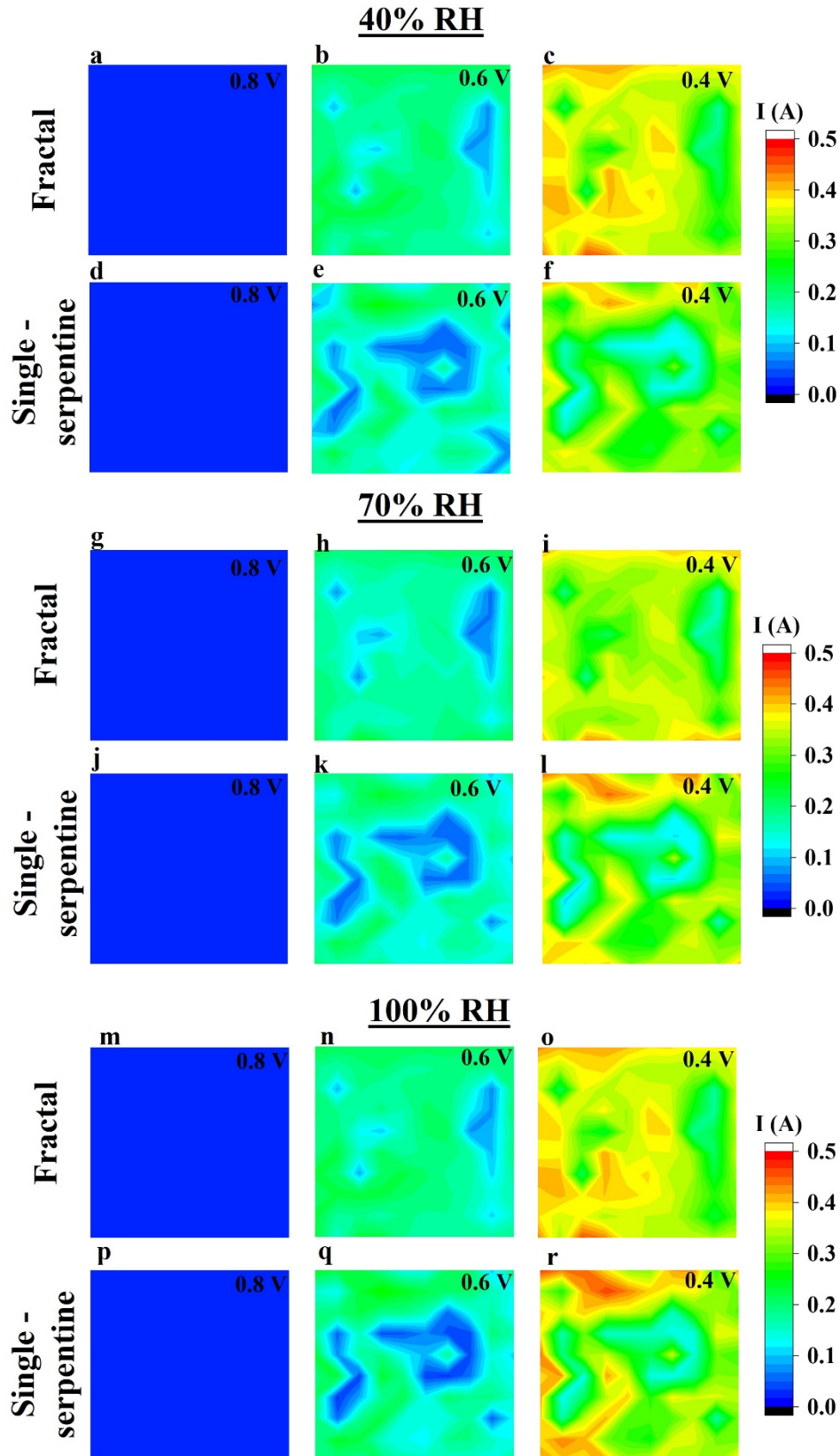369   diffusion-dominated oxygen mass transport [9].

370   *Table 2: Charge transfer resistances (Rct) and mass transfer resistances (Rmt) for single-*
371   *serpentine cell and fractal cell at 0.8 A cm^{-2} and 1 A cm^{-2}, for 40%, 70% and 100% RH reactant*
372   *conditions.*

		Single-serpentine			Fractal		
		40% RH	70% RH	100% RH	40% RH	70% RH	100% RH
R_{ct} (Ω cm^2)	@ 0.8 A cm^{-2}	0.207	0.175	0.221	0.189	0.147	0.138
	@ 1 A cm^{-2}	0.194	0.172	0.225	0.188	0.136	0.123
R_{mt} (Ω cm^2)	@ 0.8 A cm^{-2}	0.015	0.024	0.041	0.006	0.012	0.015
	@ 1 A cm^{-2}	0.016	0.024	0.046	0.008	0.015	0.016

373

374   **3.5 Current distribution analysis**

375   Current distribution maps at 40%, 70% and 100% reactant RH are presented in Fig. 7, where

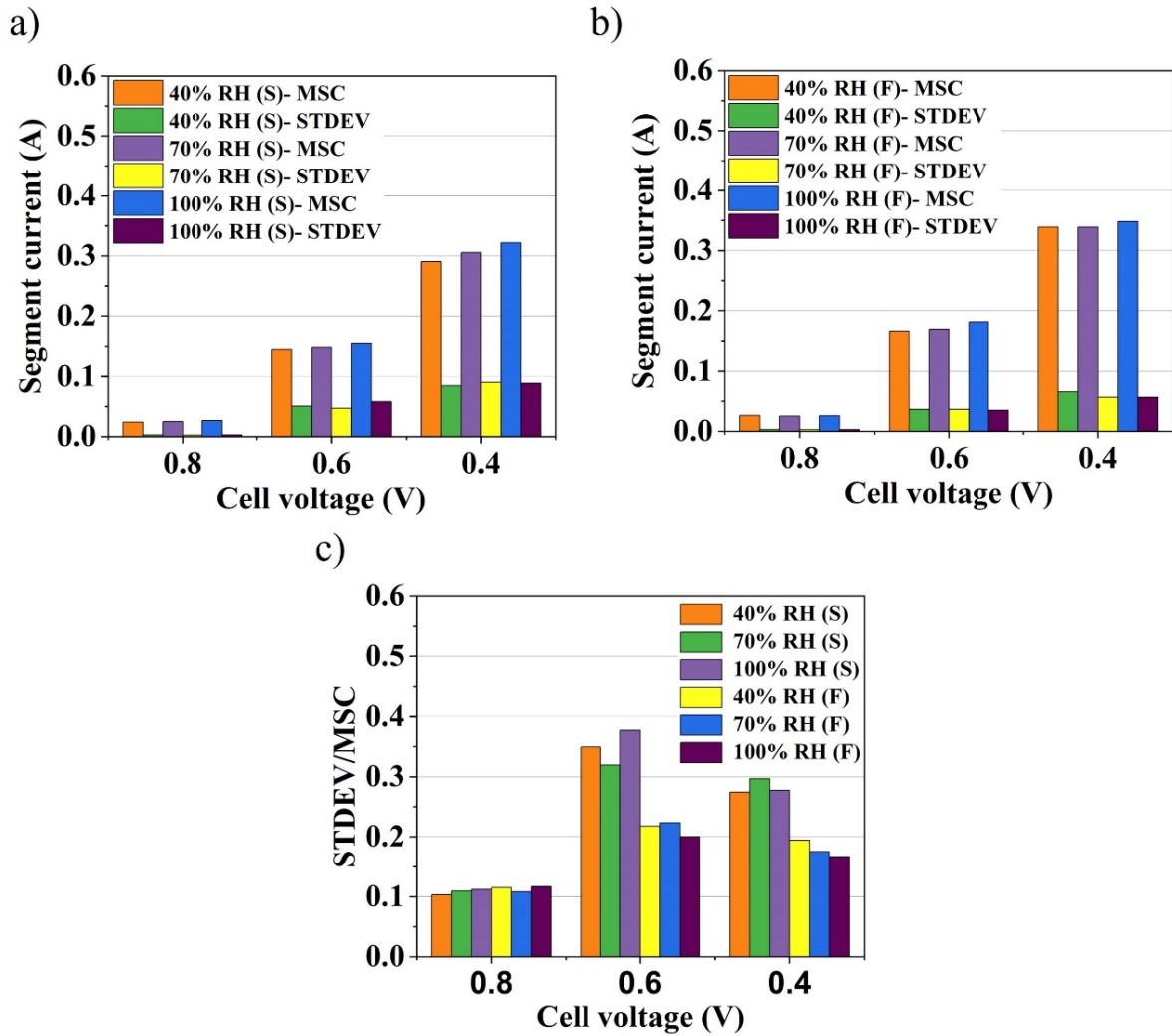376   the maps (a-c), (g-i) and (m-o) correspond to the fractal cell and (d-f), (j-l) and (p-r)

Figure 7: Current distribution for fractal cell at (a-c) 40% RH, (g-i) 70% RH and (m-o) 100% RH, and for single-serpentine cell at (d-f) 40% RH, (j-l) 70% RH and (p-r) 100% RH. Cell voltage for (a, d, g , j, m, p) is 0.8 V, for (b, e, h, k, n, q) it is 0.6 V and for (c, f, i, l, o, r) it is 0.4 V.

381 correspond to the single-serpentine cell. The maps in Fig. 7 represent the local currents

382 measured by the 10 × 10 shunt resistors (segments) on the current mapping plate, as shown

383 in Fig. S4. A schematic representation of the cathode flow-fields, with respect to the current

384 mapping segments, is given in Fig. S5.

385 At 0.8 V cell voltage, it can be observed from the maps in Fig. 7 that, irrespective of the

386 reactant RH condition, a similar and uniform current distribution is measured in both single-

387 serpentine and fractal cells. Furthermore, the mean of segment currents (MSC), an average

388 of the overall segment currents measured, and the corresponding standard deviation

389 (STDEV), representing variations in segment currents from the MSC, are given in Figs. 8 (a-b),

390 and the corresponding MSC and STDEV at 0.8 V for both cell designs are similar at ≈ 0.025 A

391 and ≈ 0.003 A, respectively.

Figure 8: Mean of segment currents (MSC) and its corresponding standard deviation (STDEV) for fuel cells with (a) a single-serpentine flow-field (S) and (b) a fractal flow-field (F), at 40%, 70% and 100% reactant RH, and (c) normalised STDEV with respect to the MSC for the same.

In addition, the normalised STDEV (STDEV/MSC) for both cells are almost the same, indicating similar levels of dispersion of segment current around the MSC, as shown in Fig. 8 (c). This is supported by the segment current distribution about the MSC at 0.8 V, as shown in Fig.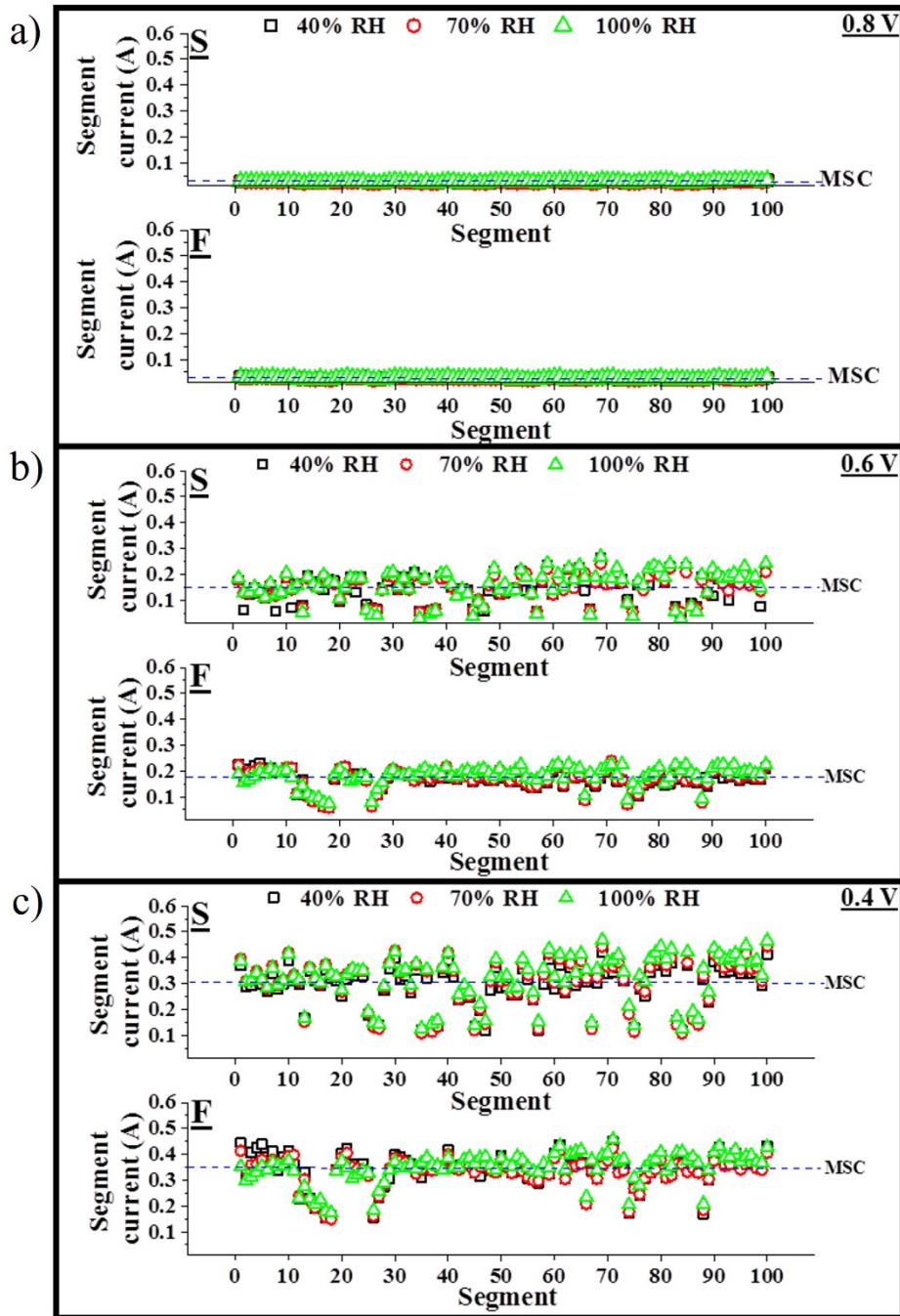 9, which indicates uniform current development across all 100 segments (segment-wise representation on the current maps is shown in Fig. S5). Furthermore, Fig. S6 represents the uniformity of the current distribution as a function of cell voltage, but with different current scales adjusted for each cell voltage and the segment wise current distribution across the 10 x 10 segments.

404

Figure 9: Segment current distribution at (a) 0.8 V cell voltage, (b) 0.6 V cell voltage and (c) 0.4 V cell voltage. Legend: MSC – mean segment current, S – single-serpentine, F – fractal.

These imply that the overall current distribution is uniform across segments in both cells at

low operating currents [23,50]. Such homogeneity in the current distribution, at higher cell

voltages, can be attributed to the negligible diffusion limitations, since the intrinsic rate of

reaction and current are low, with minimal impact from water dynamics and reactant

411   concentration [22,37]. Here, the observed similarities in current distribution between the

412   cells corroborate with the polarisation performances observed in Fig. 4, where, at 0.8 V, each

413   cell delivered an output of $\approx$ 0.1 A cm^{-2} = (100 $\times$ 0.025 A)/25 cm^2.
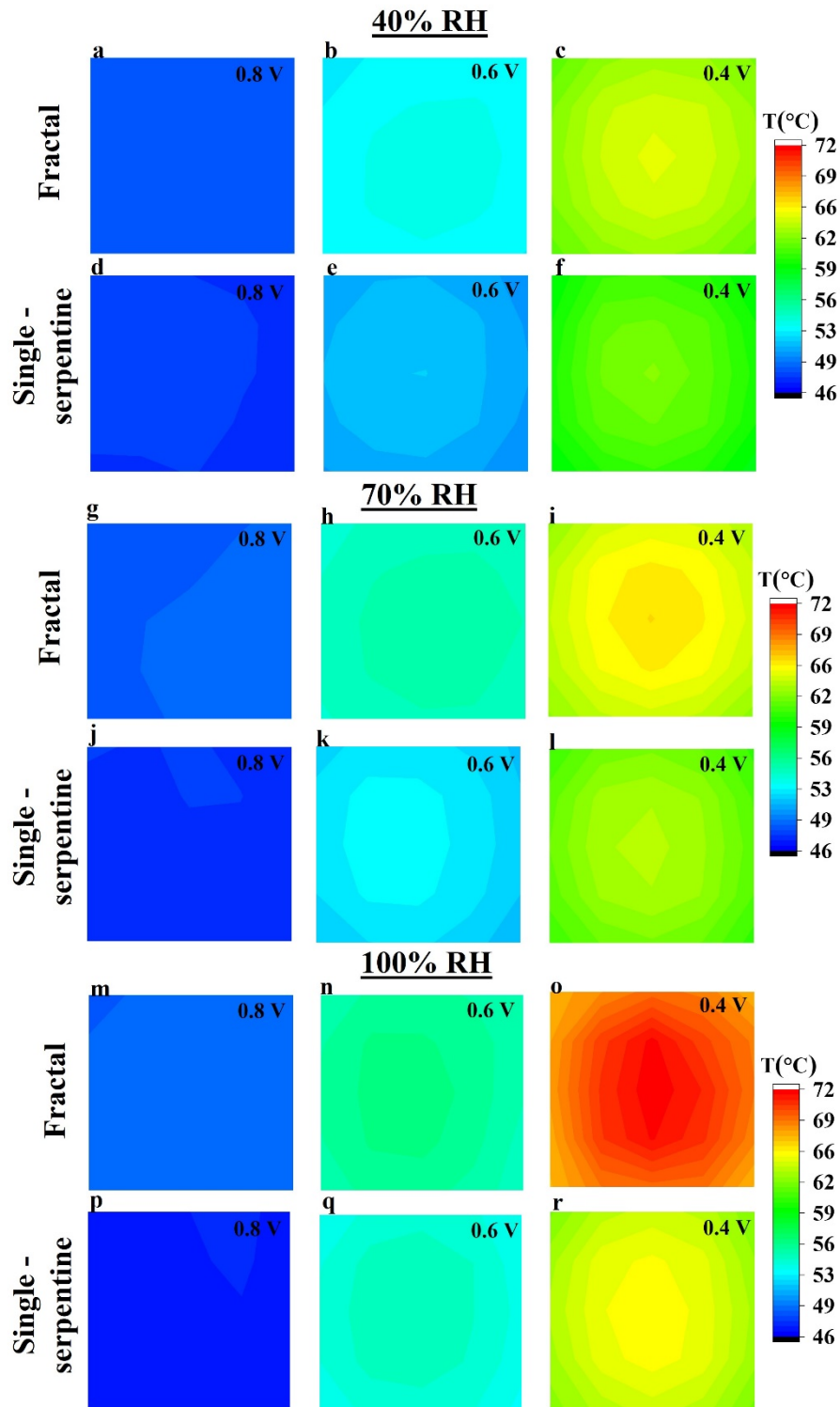
414   However, at lower cell voltages, the current distribution is inhomogeneous, as seen in Fig. 7,

415   which can be attributed to diffusion limitations at the corresponding higher average currents.

416   Prominent low-current regions, seen as deep blue patches in Fig. 7, developed to a larger

417   extent in the single-serpentine cell. Comparatively, the fractal cell developed a more uniform

418   current distribution. Besides, the fractal cell is observed to have a higher MSC and lower

419   STDEV compared to the single-serpentine cell, as shown in Figs. 8 (a-b). The corresponding

420   normalised STDEV in Fig. 8 (c) is also lower for the fractal cell, confirming lower levels of

421   dispersion of segment currents around the MSC. However, the greater extent of low-current

422   regions in a single-serpentine cell likely results from relatively excessive reactant starvation

423   in these regions, due to localised flooding or excess water retention [51–53]. This is supported

424   by the higher levels of dispersion of segment currents around the MSC, as established by the

425   normalised STDEV shown Fig. 8 (c). The corresponding segment current distribution (100

426   segments) around the MSC, at 0.6 V and 0.4 V cell potentials, is given in Fig. 9, which highlights

427   the development of low and high segment currents in each cell. However, the number of such

428   segments varies, depending on the cathode flow-field type used (note again that a single-

429   serpentine anode flow-field was used in both cases). In particular, the number of low current

430   segments developed in a fractal cell is much lower than that in a single-serpentine cell under

431   any condition, consistent with a lower normalised STDEV in Fig. 8 (c). For instance, $\approx$ 8 – 10

432   segments in a fractal cell and $\approx$ 18 – 20 segments in a single-serpentine cell develop a current

25

433 less than 0.1 A at 0.6 V, and 0.2 A at 0.4 V, respectively (the currents here correspond to the

434 value for MSC-STDEV for a single-serpentine cell at the corresponding voltage).

435 Overall, the observed better performance with more homogeneous current distribution for

436 the fractal cell can be attributed to the uniform reactant and water distribution occurring

437 from the fractal flow-field structure. In addition, the better performance of the fractal cell

438 identified here corroborates the corresponding polarisation performances, given in Table 1.

439 **3.6 Surface temperature distribution analysis**

440 The corresponding anode surface temperature distribution, indicative of the local internal cell

441 temperatures in the fractal and the single-serpentine cells, is given in Fig. 10. Here, the

442 hydration conditions generated inside the cell and their influence on the corresponding

443 surface temperature are explored. The surface temperatures measured at the central

444 segment of the mapping plate (at the centre of the anode surface) for the fractal cell at 0.6 V

445 are 53.4 ^{o}C (40% RH), 55 ^{o}C (70% RH) and 56.1 ^{o}C (100% RH), and at 0.4 V are 64.6 ^{o}C (40%

446 RH), 66.1 ^{o}C (70% RH) and 71.9 ^{o}C (100% RH). Corresponding central segment temperatures

447 for the single-serpentine cell at 0.6 V are 51.4 ^{o}C (40% RH), 52.8 ^{o}C (70% RH) and 54.5 ^{o}C

448 (100% RH) and at 0.4 V are 62.4 ^{o}C (40% RH), 63.6 ^{o}C (70% RH) and 65.4 ^{o}C (100% RH),

449 respectively. It is clear that the fractal cell developed much higher surface temperatures in

450 the central segment of the anode plate compared to the single-serpentine cell, irrespective

451 of reactant RH and cell operating voltage, corroborating the cell temperatures measured

452 using a thermocouple during polarisation curve measurements, as given in Fig. 5.

Figure 10: Temperature distribution for fractal cell at (a-c) 40% RH, (g-i) 70% RH and (m-o) 100% RH, and for single-serpentine cell at (d-f) 40% RH, (j-l) 70% RH and (p-r) 100% RH. Cell voltage for (a, d, g, j, m, p) is 0.8 V, for (b, e, h, k, n, q) it is 0.6 V and for (c, f, i, l, o, r) it is 0.4 V.

458   Besides, the surface temperatures are 4 – 5 °C lower than the cell temperatures measured

459   using the thermocouple, across all operating conditions. This can be attributed to the

460   proximity of the thermocouple to the MEA region, in addition to the heat loss occurring to

461   the ambient surroundings.

462   With continuous heat dissipation to the surroundings at the edges of the cell, the temperature

463   is higher in the cell centre and lower at the edges, as seen in Fig. 10 [38,54,55].The differences

464   between the centre and edge surface temperatures are similar for both cells: ~0.2-3 ^{o}C, ~1-2

465   ^{o}C at 0.6 V and ~3-4 ^{o}C at 0.4 V, irrespective of the reactant conditions, indicating that there

466   is a consistent temperature gradient or heat distribution on the cell surface for a given current

467   density under the range of conditions studied.

468   The lower surface temperatures measured in the single-serpentine cell can be attributed to

469   the reduced rate of heat dissipation compared to the fractal cell. Another contributing factor

470   is the localised flooding occurring in the single-serpentine cell, especially on the GDL surface,

471   which reduces the effective catalyst area available for the electrochemical reactions to occur,

472   and results in decreased current density and associated generated heat [56].

473   **4. Conclusions**

474   An electro-thermal mapping approach has been applied to derive original insights into the

475   reasons for improved performance of a cathode fractal flow-field compared to a conventional

476   serpentine flow-field for a PEMFC. The study establishes a relationship between cell

477   performance and the surface distribution of current and temperature. It also provides an

478   understanding of localised phenomena, such as flooding occurring because of the flow-field

479   configuration.

480   X-ray CT scan analysis demonstrates the layer-wise PCB-based assembly as an effective

481   approach for developing the fractal flow-fields. The fractal fuel cell delivered better

482   performance, especially in the high current density region, compared to the single-serpentine

483   cell, over a range of reactant RH and operating conditions. The enhanced performance of the

484   fractal cell is a result of higher cell temperatures developed in the fractal cell compared to the

485   single-serpentine cell. Uniform and stable Ohmic resistances, over the polarisation range, are

486   measured for both cells, indicating well-hydrated membrane conditions throughout

487   operation. In addition, electrochemical impedance spectroscopy measurements are

488   consistent with stable and flooded operating conditions in the fractal and the single-

489   serpentine cells, respectively.

490   Relatively homogeneous current distribution is observed in the fractal cell as a result of more

491   uniform reactant and water distribution, while a more non-uniform current distribution is

492   developed in the single-serpentine cell as a result of flooding conditions. The superior

493   performance of the fractal cell is reflected by the segment currents measured, which are ≈

494   10-15% higher than those measured in the single-serpentine cell. This is consistent with the

495   higher surface temperature distribution observed for the fractal cell as a result of the higher

496   current density.

497   Finally, this study further asserts, via electrothermal metrology, the water and thermal

498   management benefits in fuel cells when using a nature-inspired approach, compared to

499   conventional fuel cells.

500

501

5. References

[1]   L. Barelli, G. Bidini, F. Gallorini, A. Ottaviano, An energetic-exergetic analysis of a residential CHP system based on PEM fuel cell, Appl. Energy. 88 (2011) 4334–4342. doi:10.1016/j.apenergy.2011.04.059.

[2]   F. Barbir, T. Gómez, Efficiency and economics of proton exchange membrane (PEM) fuels cells, Int. J. Hydrogen Energy. 21 (1996) 891–901. doi:10.1016/0360-3199(96)00030-4.

[3]   X. Li, I. Sabir, Review of bipolar plates in PEM fuel cells: Flow-field designs, Int. J. Hydrogen Energy. 30 (2005) 359–371. doi:10.1016/j.ijhydene.2004.09.019.

[4]   R. Taccani, N. Zuliani, Effect of flow field design on performances of high temperature

524   PEM fuel cells: Experimental analysis, Int. J. Hydrogen Energy. 36 (2011) 10282–

525   10287. doi:10.1016/j.ijhydene.2010.10.026.

526   [5]   D. Natarajan, T. Van Nguyen, Three-dimensional effects of liquid water flooding in the

527   cathode of a PEM fuel cell, J. Power Sources. 115 (2003) 66–80. doi:10.1016/S0378-

528   7753(02)00624-9.

529   [6]   A. Su, F.B. Weng, C.Y. Hsu, Y.M. Chen, Studies on flooding in PEM fuel cell cathode

530   channels, Int. J. Hydrogen Energy. 31 (2006) 1031–1039.

531   doi:10.1016/j.ijhydene.2005.12.019.

532   [7]   S. Kjelstrup, M.O. Coppens, J.G. Pharoah, P. Pfeifer, Nature-inspired energy-and

533   material-efficient design of a polymer electrolyte membrane fuel cell, Energy and

534   Fuels. 24 (2010) 5097–5108. doi:10.1021/ef100610w.

535   [8]   P. Trogadas, J.I.S. Cho, T.P. Neville, J. Marquis, B. Wu, D.J.L. Brett, M.O. Coppens, A

536   lung-inspired approach to scalable and robust fuel cell design, Energy Environ. Sci. 11

537   (2018) 136–143. doi:10.1039/c7ee02161e.

538   [9]   J.I.S. Cho, J. Marquis, P. Trogadas, T.P. Neville, D.J.L. Brett, M.O. Coppens, Optimizing

539   the Architecture of Lung-Inspired Fuel Cells, Chem. Eng. Sci. (2019) 115375.

540   doi:10.1016/j.ces.2019.115375.

541   [10]   V.S. Bethapudi, J. Hack, P. Trogadas, J.I.S. Cho, L. Rasha, G. Hinds, P.R. Shearing, D.J.L.

542   Brett, M.-O. Coppens, A lung-inspired printed circuit board polymer electrolyte fuel

543   cell, Energy Convers. Manag. 202 (2019) 112198.

544   doi:10.1016/j.enconman.2019.112198.

545　[11]　J.P. Kloess, X. Wang, J. Liu, Z. Shi, L. Guessous, Investigation of bio-inspired flow

546　　　　channel designs for bipolar plates in proton exchange membrane fuel cells, J. Power

547　　　　Sources. 188 (2009) 132–140. doi:10.1016/j.jpowsour.2008.11.123.

548　[12]　N. Guo, M.C. Leu, U.O. Koylu, Bio-inspired flow field designs for polymer electrolyte

549　　　　membrane fuel cells, Int. J. Hydrogen Energy. 39 (2014) 21185–21195.

550　　　　doi:10.1016/j.ijhydene.2014.10.069.

551　[13]　A. Arvay, J. French, J.C. Wang, X.H. Peng, A.M. Kannan, Nature inspired flow field

552　　　　designs for proton exchange membrane fuel cell, Int. J. Hydrogen Energy. 38 (2013)

553　　　　3717–3726. doi:10.1016/j.ijhydene.2012.12.149.

554　[14]　M.O. Coppens, A nature-inspired approach to reactor and catalysis engineering, Curr.

555　　　　Opin. Chem. Eng. 1 (2012) 281–289. doi:10.1016/j.coche.2012.03.002.

556　[15]　J. Marquis, M.O. Coppens, Achieving ultra-high platinum utilization via optimization

557　　　　of PEM fuel cell cathode catalyst layer microstructure, Chem. Eng. Sci. 102 (2013)

558　　　　151–162. doi:10.1016/j.ces.2013.08.003.

559　[16]　V.S. Bethapudi, J. Hack, P. Trogadas, G. Hinds, P.R. Shearing, D.J.L. Brett, Hydration

560　　　　state diagnosis in fractal flow-field based polymer electrolyte membrane fuel cells

561　　　　using acoustic emission analysis, Energy Convers. Manag. 220 (2020) 113083.

562　　　　doi:10.1016/j.enconman.2020.113083.

563　[17]　D.G. Strickland, S. Litster, J.G. Santiago, Current distribution in polymer electrolyte

564　　　　membrane fuel cell with active water management, J. Power Sources. 174 (2007)

565　　　　272–281. doi:10.1016/j.jpowsour.2007.08.059.

566 [18] M. Rahimi-Esbo, A.A. Ranjbar, A. Ramiar, E. Alizadeh, M. Aghaee, Improving PEM fuel

567   cell performance and effective water removal by using a novel gas flow field, Int. J.

568   Hydrogen Energy. 41 (2016) 3023–3037. doi:10.1016/j.ijhydene.2015.11.001.

569 [19] N. Rajalakshmi, M. Raja, K.S. Dhathathreyan, Evaluation of current distribution in a

570   proton exchange membrane fuel cell by segmented cell approach, J. Power Sources.

571   112 (2002) 331–336. doi:10.1016/S0378-7753(02)00352-X.

572 [20] M. Belhadj, A. Aquino, J. Heng, S. Kmiotek, S. Raël, C. Bonnet, F. Lapicque, Current

573   density distributions in polymer electrolyte fuel cells: A tool for characterisation of

574   gas distribution in the cell and its state of health, Chem. Eng. Sci. 185 (2018) 18–25.

575   doi:10.1016/j.ces.2018.03.055.

576 [21] I. Alaefour, G. Karimi, K. Jiao, S. Al Shakhshir, X. Li, Experimental study on the effect of

577   reactant flow arrangements on the current distribution in proton exchange

578   membrane fuel cells, Electrochim. Acta. 56 (2011) 2591–2598.

579   doi:10.1016/j.electacta.2010.11.002.

580 [22] Q. Zhang, R. Lin, L. Técher, X. Cui, Experimental study of variable operating

581   parameters effects on overall PEMFC performance and spatial performance

582   distribution, Energy. 115 (2016) 550–560. doi:10.1016/j.energy.2016.08.086.

583 [23] Y. Yu, X.Z. Yuan, H. Li, E. Gu, H. Wang, G. Wang, M. Pan, Current mapping of a proton

584   exchange membrane fuel cell with a segmented current collector during the gas

585   starvation and shutdown processes, Int. J. Hydrogen Energy. 37 (2012) 15288–15300.

586   doi:10.1016/j.ijhydene.2012.07.023.

587 [24] Y. Vazifeshenas, K. Sedighi, M. Shakeri, Numerical investigation of a novel compound

33

588   flow-field for PEMFC performance improvement, Int. J. Hydrogen Energy. 40 (2015)

589   15032–15039. doi:10.1016/j.ijhydene.2015.08.077.

590   [25] Q. Meyer, K. Ronaszegi, J.B. Robinson, M. Noorkami, O. Curnick, S. Ashton, A.

591   Danelyan, T. Reisch, P. Adcock, R. Kraume, P.R. Shearing, D.J.L. Brett, Combined

592   current and temperature mapping in an air-cooled, open-cathode polymer electrolyte

593   fuel cell under steady-state and dynamic conditions, J. Power Sources. 297 (2015)

594   315–322. doi:10.1016/j.jpowsour.2015.07.069.

595   [26] B.D. Gould, R. Ramamurti, C.R. Osland, K.E. Swider-Lyons, Assessing fuel-cell coolant

596   flow fields with numerical models and infrared thermography, Int. J. Hydrogen

597   Energy. 39 (2014) 14061–14070. doi:10.1016/j.ijhydene.2014.07.018.

598   [27] H. Shao, D. Qiu, L. Peng, P. Yi, X. Lai, In-situ measurement of temperature and

599   humidity distribution in gas channels for commercial-size proton exchange

600   membrane fuel cells, J. Power Sources. 412 (2019) 717–724.

601   doi:10.1016/j.jpowsour.2018.12.008.

602   [28] R. Vijayakumar, T. Ramkumar, S. Maheswari, P. Sridhar, S. Pitchumani, Current and

603   clamping pressure distribution studies on the scale up issues in direct methanol fuel

604   cells, Electrochim. Acta. 90 (2013) 274–282. doi:10.1016/j.electacta.2012.11.129.

605   [29] L. Peng, H. Shao, D. Qiu, P. Yi, X. Lai, Investigation of the non-uniform distribution of

606   current density in commercial-size proton exchange membrane fuel cells, J. Power

607   Sources. 453 (2020) 227836. doi:10.1016/j.jpowsour.2020.227836.

608   [30] M. Wilkinson, M. Blanco, E. Gu, J.J. Martin, D.P. Wilkinson, J.J. Zhang, H. Wang, In Situ

609   Experimental Technique for Measurement of Temperature and Current Distribution

610   in Proton Exchange Membrane Fuel Cells, Electrochem. Solid-State Lett. 9 (2006)

611   A507. doi:10.1149/1.2338769.

612   [31] C. Wieser, A. Helmbold, E. Gülzow, New technique for two-dimensional current

613   distribution measurements in electrochemical cells, J. Appl. Electrochem. 30 (2000)

614   803–807. doi:10.1023/A:1004047412066.

615   [32] A. Hakenjos, C. Hebling, Spatially resolved measurement of PEM fuel cells, J. Power

616   Sources. 145 (2005) 307–311. doi:10.1016/j.jpowsour.2005.01.075.

617   [33] S.A. Freunberger, M. Reum, J. Evertz, A. Wokaun, F.N. Büchi, Measuring the current

618   distribution in PEFCs with sub-millimeter resolution, J. Electrochem. Soc. 153 (2006)

619   2158–2165. doi:10.1149/1.2345591.

620   [34] G. Zhang, L. Guo, L. Ma, H. Liu, Simultaneous measurement of current and

621   temperature distributions in a proton exchange membrane fuel cell, J. Power Sources.

622   195 (2010) 3597–3604. doi:10.1016/j.jpowsour.2009.12.016.

623   [35] A. Hakenjos, H. Muenter, U. Wittstadt, C. Hebling, A PEM fuel cell for combined

624   measurement of current and temperature distribution, and flow field flooding, J.

625   Power Sources. 131 (2004) 213–216. doi:10.1016/j.jpowsour.2003.11.081.

626   [36] S.S. Hsieh, Y.J. Huang, Measurements of current and water distribution for a micro-

627   PEM fuel cell with different flow fields, J. Power Sources. 183 (2008) 193–204.

628   doi:10.1016/j.jpowsour.2008.04.065.

629   [37] I. Alaefour, G. Karimi, K. Jiao, X. Li, Measurement of current distribution in a proton

630   exchange membrane fuel cell with various flow arrangements - A parametric study,

631   Appl. Energy. 93 (2012) 80–89. doi:10.1016/j.apenergy.2011.05.033.

632   [38] C. Minnaar, F. De Beer, D. Bessarabov, Current Density Distribution of Electrolyzer

633   Flow Fields: In Situ Current Mapping and Neutron Radiography, Energy & Fuels. 34

634   (2019) 1014–1023. doi:10.1021/acs.energyfuels.9b03814.

635   [39] J.I.S. Cho, T.P. Neville, P. Trogadas, Q. Meyer, Y. Wu, R. Ziesche, P. Boillat, M. Cochet,

636   V. Manzi-Orezzoli, P. Shearing, D.J.L. Brett, M.-O. Coppens, Visualization of Liquid

637   Water in a Lung-Inspired Flow-Field based Polymer Electrolyte Membrane Fuel Cell

638   via Neutron Radiography, Energy. 170 (2018) 14–21.

639   doi:10.1016/J.ENERGY.2018.12.143.

640   [40] S. Gheorghiu, . Kjelstrup, P. Pfeifer3, M.-O. Coppens, Is the Lung an Optimal Gas

641   Exchanger?, in: G.A. Losa, D. Merlini, T.F. Nonnenmacher, E.R. Weibel (Eds.), Fractals

642   Biol. Med., Birkhäuser Basel, Basel, 2006: pp. 31–42. https://doi.org/10.1007/3-7643-

643   7412-8_3.

644   [41] K. Nishida, T. Murakami, S. Tsushima, S. Hirai, Measurement of liquid water content

645   in cathode gas diffusion electrode of polymer electrolyte fuel cell, J. Power Sources.

646   195 (2010) 3365–3373. doi:10.1016/j.jpowsour.2009.12.073.

647   [42] R.M. Aslam, D.B. Ingham, M.S. Ismail, K.J. Hughes, L. Ma, M. Pourkashanian,

648   Simultaneous thermal and visual imaging of liquid water of the PEM fuel cell flow

649   channels, J. Energy Inst. 92 (2019) 311–318. doi:10.1016/j.joei.2018.01.005.

650   [43] G. Karimi, F. Jafarpour, X. Li, Characterization of flooding and two-phase flow in

651   polymer electrolyte membrane fuel cell stacks, J. Power Sources. 187 (2009) 156–164.

652   doi:10.1016/j.jpowsour.2008.10.108.

653   [44]   K.R. Cooper, M. Smith, Electrical test methods for on-line fuel cell ohmic resistance

654   measurement, J. Power Sources. 160 (2006) 1088–1095.

655   doi:10.1016/j.jpowsour.2006.02.086.

656   [45]   A. Hakenjos, M. Zobel, J. Clausnitzer, C. Hebling, Simultaneous electrochemical

657   impedance spectroscopy of single cells in a PEM fuel cell stack, J. Power Sources. 154

658   (2006) 360–363. doi:10.1016/j.jpowsour.2005.10.055.

659   [46]   H.D. Ham, Influence of the water content on the kinetics of counter-ion transport in

660   pefiuorosulphonic membranes, J Electroanal Chem 1998;287:43–59.

661   https://doi.org/10.1016/0022-0728(90)87159-H.

662   [47]   Y. Wu, J.I.S. Cho, T.P. Neville, Q. Meyer, R. Zeische, P. Boillat, M. Cochet, P.R.

663   Shearing, D.J.L. Brett, Effect of serpentine flow-field design on the water

664   management of polymer electrolyte fuel cells: An in-operando neutron radiography

665   study, J. Power Sources. 399 (2018) 254–263. doi:10.1016/j.jpowsour.2018.07.085.

666   [48]   O.A. Obeisun, Q. Meyer, J. Robinson, C.W. Gibbs, A.R. Kucernak, P.R. Shearing, D.J.L.

667   Brett, Development of open-cathode polymer electrolyte fuel cells using printed

668   circuit board flow-field plates: Flow geometry characterisation, Int. J. Hydrogen

669   Energy. 39 (2014) 18326–18336. doi:10.1016/j.ijhydene.2014.08.106.

670   [49]   R. O'Hayre, T. Fabian, S. Litster, F.B. Prinz, J.G. Santiago, Engineering model of a

671   passive planar air breathing fuel cell cathode, J. Power Sources. 167 (2007) 118–129.

672   doi:10.1016/j.jpowsour.2007.01.073.

673   [50]   D.J.L. Brett, S. Atkins, N.P. Brandon, V. Vesovic, N. Vasileiadis, A. Kucernak, Localized

674   impedance measurements along a single channel of a solid polymer fuel cell,

675   Electrochem. Solid-State Lett. 6 (2003) 110–113. doi:10.1149/1.1557034.

676   [51]   H. Sun, G. Zhang, L.J. Guo, S. Dehua, H. Liu, Effects of humidification temperatures on

677   local current characteristics in a PEM fuel cell, J. Power Sources. 168 (2007) 400–407.

678   doi:10.1016/j.jpowsour.2007.03.022.

679   [52]   F. Barbir, H. Gorgun, X. Wang, Relationship between pressure drop and cell resistance

680   as a diagnostic tool for PEM fuel cells, J. Power Sources. 141 (2005) 96–101.

681   doi:10.1016/j.jpowsour.2004.08.055.

682   [53]   J. Stumper, M. Löhr, S. Hamada, Diagnostic tools for liquid water in PEM fuel cells, J.

683   Power Sources. 143 (2005) 150–157. doi:10.1016/j.jpowsour.2004.11.036.

684   [54]   C.Y. Wen, Y.S. Lin, C.H. Lu, Performance of a proton exchange membrane fuel cell

685   stack with thermally conductive pyrolytic graphite sheets for thermal management, J.

686   Power Sources. 189 (2009) 1100–1105. doi:10.1016/j.jpowsour.2008.12.103.

687   [55]   L. Luo, Q. Jian, B. Huang, Z. Huang, J. Zhao, S. Cao, Experimental study on

688   temperature characteristics of an air-cooled proton exchange membrane fuel cell

689   stack, Renew. Energy. 143 (2019) 1067–1078. doi:10.1016/j.renene.2019.05.085.

690   [56]   D.N. Ozen, B. Timurkutluk, K. Altinisik, Effects of operation temperature and reactant

691   gas humidity levels on performance of PEM fuel cells, Renew. Sustain. Energy Rev. 59

692   (2016) 1298–1306. doi:10.1016/j.rser.2016.01.040.

693